

Quantitatively predicting angle-resolved polarized Raman intensity of black phosphorus flakes

Tao Liu^{1,2,†}, Jia-Liang Xie^{1,2,‡}, Yu-Chen Leng¹, Heng Wu^{1,2}, Jiahong Wang³, Yang Li³, Xue-Feng Yu³, Miao-Ling Lin^{1*} and Ping-Heng Tan^{1,2,†}
¹ State Key Laboratory of Superlattices and Microstructures,
Institute of Semiconductors, Chinese Academy of Sciences, Beijing 100083, China

² Center of Materials Science and Optoelectronics Engineering &
CAS Center of Excellence in Topological Quantum Computation,
University of Chinese Academy of Sciences, Beijing, 100049, China

³ Shenzhen Engineering Center for the Fabrication of Two-Dimensional Atomic Crystals,
Shenzhen Institutes of Advanced Technology, Chinese Academy of Sciences, Shenzhen 518055, China and
[†] Contributed equally to this work

In-plane anisotropic layered materials (ALMs), such as black phosphorus (BP), exhibit unique angle-resolved polarized Raman (ARPR) spectroscopy characteristics, as attributed to birefringence, linear dichroism and complex Raman tensor. Moreover, the ARPR intensity profiles of BP flakes deposited on multilayer dielectrics are notably sensitive to their thickness, owing to interference effects. The intricate anisotropic effects present challenges in accurately predicting the ARPR intensity of BP flakes. In this study, we propose a comprehensive strategy for predicting the ARPR intensity of BP flakes by explicitly considering optical anisotropy, encompassing birefringence, linear dichroism, and anisotropic cavity interference effects within multilayered structures. Through this approach, we have identified the intrinsic complex Raman tensors for phonon modes, independent of the BP flake thickness. By leveraging this methodology, we have elucidated the flake thickness-dependent effective complex Raman tensor elements, allowing for precise prediction of the observed ARPR intensity profile for the BP flake. This work provides a profound understanding of ARPR behaviors for ALM flakes.

Raman scattering intensity in general depends on the direction of incident laser and collected Raman light relative to the principal axes of the crystal[1], whose polarization vectors are \mathbf{e}_i and \mathbf{e}_s , respectively. The Raman tensor (\mathbf{R} with 3×3 tensor elements R_{uv} , $u, v = x, y, z$) serves as a crucial component in determining the Raman intensity by $I \propto |\mathbf{e}_s \cdot \mathbf{R} \cdot \mathbf{e}_i|^2$ (Fig.1(a1))[1]. Once the phonon symmetry is known, the Raman selection rule for the corresponding Raman mode can be experimentally verified[1, 2], determining whether it is observed or not. By altering the direction of \mathbf{e}_i and \mathbf{e}_s with respect to the crystallographic axes, angle-resolved polarized Raman (ARPR) intensity can be estimated[1, 3–6]. In most cases, only real Raman tensor is generally involved to deduce a formalism for calculating Raman scattering intensity dependent on the polarization configuration for bulk crystals[3–5]. However, in H.B. Ribeiro’s pioneering work[6], the unusual ARPR spectra were observed in black phosphorus (BP) flakes (360nm thickness), which can be explained only by considering complex Raman tensor. Then, huge efforts were made to understand the ARPR intensity profile of anisotropic layered materials (ALMs) after taking birefringence and linear dichroism effects into account in detail[5–18]. The fitted \mathbf{R} (amplitude ratio and phase difference between two tensor elements) were found to be sensitive to the flake thickness and the layer thickness of substrate dielectrics[6–14],

making it impossible to predict ARPR spectrum for BP flakes with different thickness and on different substrate.

In principle, Raman tensor is an inherent parameter for a crystal to understand its Raman spectrum [1, 3, 19], regardless of its volume[20], dimensionality[21, 22] and even its counterpart[20, 23] in multilayer dielectrics. For ALMs, such as BP flakes[24–28], the birefringence and linear dichroism effects result in depth (y)-dependent polarization and intensity of both excitation and scattered light[5]. This leads to y -dependent polarization vectors $\mathbf{e}'_s(y)$ and $\mathbf{e}'_i(y)$ [5], which cannot be approximately treated as constants of \mathbf{e}_s and \mathbf{e}_i (Fig.1(a2))[5, 29–32], respectively. Therefore, it is crucial to unveil the intrinsic Raman tensor \mathbf{R}_{int} correlated with $\mathbf{e}'_s(y)$ and $\mathbf{e}'_i(y)$ to estimate Raman intensity at the location of the scattering event at depth y within BP flakes by $I(y) \propto |\mathbf{e}'_s(y) \cdot \mathbf{R}_{\text{int}} \cdot \mathbf{e}'_i(y)|^2$. Flake-substrate multilayer dielectrics can further modulate the light propagation within BP flakes due to the interference effects of excitation/scattered light[20, 33]. How to extract \mathbf{R}_{int} in all the experimental scenes to quantitatively predict the ARPR response of BP flakes is thus a major challenge in this field.

In this letter, we have formulated an approach to extract \mathbf{R}_{int} of BP by analyzing ARPR intensity profiles of BP flakes with different thickness deposited on 90nm-SiO₂/Si substrate. The light propagation within a BP flake modulated from optical anisotropy involving birefringence, linear dichroism and interference effects in air/BP/90nm-SiO₂/Si multilayers are fully taken into account. The experimental complex \mathbf{R}_{int} can be used to

* linmiaoling@semi.ac.cn

† phtan@semi.ac.cn

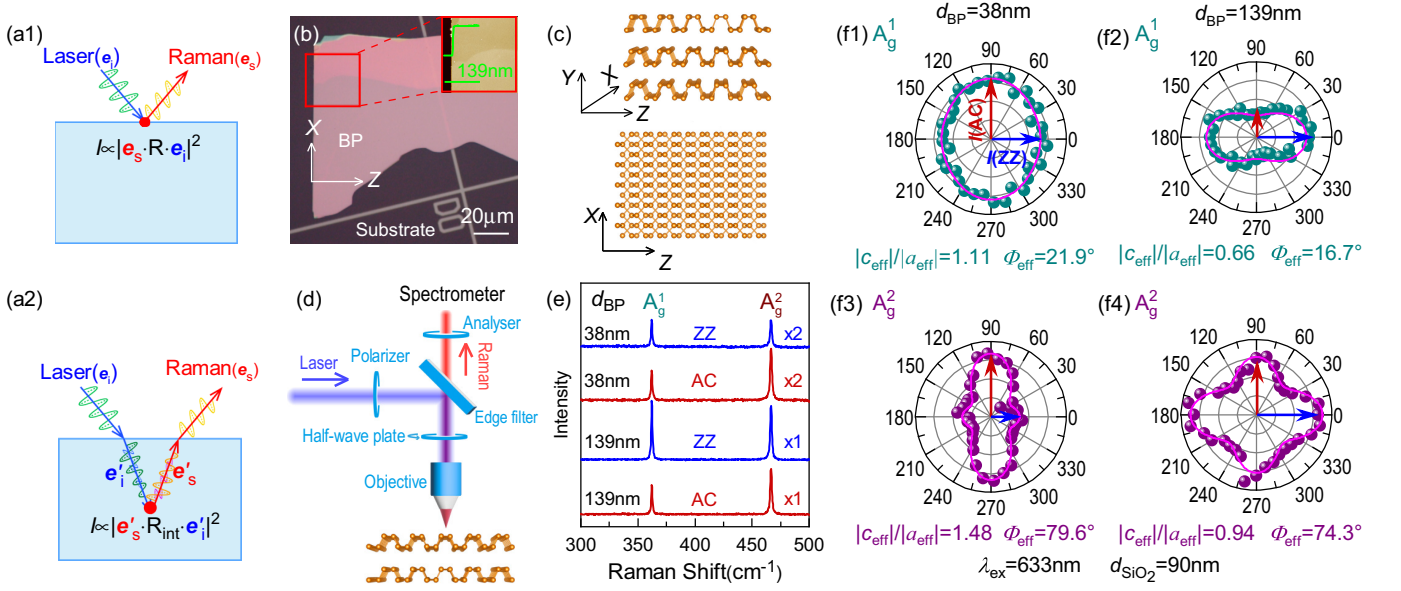


FIG. 1. (a1) Schematic diagram of Raman scattering event expressed by Raman tensor \mathbf{R} . (a2) Schematic diagram of Raman scattering event within ALM governed by \mathbf{R}_{int} , the case of oblique incidence for convenience. (b) Optical image of BP flake with $d_{BP}=139\text{nm}$ measured by AFM (inset). (c) Crystallographic structure of BP from the side and top views. (d) Schematic diagram of ARPR spectroscopy setup. (e) Raman spectra of BP flakes with $d_{BP}=38\text{nm}$ and 139nm on $90\text{nm-SiO}_2/\text{Si}$ substrate, when \mathbf{e}_i (\mathbf{e}_s) is along the ZZ and AC axes, and (f) the corresponding ARPR intensity profiles of the A_g^1 and A_g^2 modes, $\lambda_{ex}=633\text{nm}$, and the fitted $|c_{eff}|/|a_{eff}|$ and Φ_{eff} are indicated.

quantitatively reproduce ARPR intensity profile of BP flakes on $305\text{nm-SiO}_2/\text{Si}$ substrate without fitting parameters. We also generated contour plots to visualize the correlation between effective Raman tensor elements and the variations in BP flake thickness (d_{BP}) and SiO_2 layer thickness (d_{SiO_2}) at three common laser wavelengths. This framework can be extended to other ALM flakes deposited on dielectric substrate to determine the Raman tensors for fully predicting their ARPR response.

BP flakes were mechanically exfoliated (Section 1 of the Supplementary Materials (SM)) onto SiO_2/Si substrates with $d_{\text{SiO}_2}=90\text{nm}$ and 305nm . Figure 1(b) shows the optical image of BP flakes with $d_{BP} \sim 139\text{nm}$, as measured by atomic force microscopy (AFM). BP is a van der Waals semiconductor with strong in-plane anisotropy along the zigzag (ZZ) and armchair (AC) axes, belonging to the orthorhombic symmetry (i.e., D_{2h} point symmetry). We establish the X and Z axes alignment with the ZZ and AC directions[5], respectively (Fig.1(c)). We utilized the Raman setup in Fig.1(d) to measure the ARPR response of BP flakes at normal laser incidence on the basal plane under a parallel polarization configuration (Section 1 of SM). The \mathbf{e}_i and \mathbf{e}_s relative to the ZZ axis (θ) are controlled by the half-wave plate in the common optical path to measure ARPR intensity of BP flakes, with $\theta = 0^\circ$ for \mathbf{e}_i (\mathbf{e}_s) \parallel ZZ axis and $\theta = 90^\circ$ for \mathbf{e}_i (\mathbf{e}_s) \parallel AC axis. In this case, $\mathbf{e}_i = \mathbf{e}_s = (\cos\theta, 0, \sin\theta)$. Figure 1(e) plots the Raman spectra of BP flakes with $d_{BP}=38\text{nm}$ and 139nm for \mathbf{e}_i (\mathbf{e}_s) \parallel ZZ and \mathbf{e}_i (\mathbf{e}_s) \parallel AC, where two typical Raman modes, i.e., A_g^1 and A_g^2 modes

are observed at 362 cm^{-1} and 466 cm^{-1} , respectively. The Raman intensity ratio of A_g^1 (A_g^2) mode between \mathbf{e}_i (\mathbf{e}_s) \parallel ZZ ($I(\text{ZZ})$) and \mathbf{e}_i (\mathbf{e}_s) \parallel AC ($I(\text{AC})$) varied with d_{BP} , as depicted in the ARPR intensity (Fig.1(f)). The nonzero tensor elements R_{uv} for A_g mode are $R_{xx} = a$, $R_{yy} = b$, $R_{zz} = c$. Due to the normal incidence onto the basal plane, only a and c are involved. By utilizing \mathbf{R} with effective complex tensor elements, $a = |a_{eff}|e^{i\Phi_a}$ and $c = |c_{eff}|e^{i\Phi_c}$ ($\Phi_{eff} = \Phi_c - \Phi_a$)[6–9, 12, 14, 18], one can connect the experimentally measured ARPR intensity with \mathbf{e}_s and \mathbf{e}_s by $I \propto |\mathbf{e}_s \cdot \mathbf{R} \cdot \mathbf{e}_i|^2$, i.e.,

$$I \propto |a_{eff}|^2 \cos^4\theta + |c_{eff}|^2 \sin^4\theta + 2|a_{eff}||c_{eff}|\sin^2\theta \cos^2\theta \cos\Phi_{eff}. \quad (1)$$

By fitting the ARPR intensity with the Eq.1, $|c_{eff}|/|a_{eff}|$ and Φ_{eff} can be obtained. The fitted Φ_{eff} are different for A_g^1 and A_g^2 modes and vary with d_{BP} for each Raman mode. This contradicts the physical mechanism based on either birefringence[8], linear dichroism effects[6] or anisotropic electron-photon (e-pht) and electron-phonon (e-phn) couplings[9]. If Φ_{eff} only originates from the impacts of birefringence and linear dichroism on \mathbf{e}_i and \mathbf{e}_s , the Φ_{eff} for A_g^1 and A_g^2 modes[8] in a BP flake should be equal; if Φ_{eff} only arises from the anisotropic e-pht and e-phn couplings[9, 18], the relatively fixed electronic band structure[24] for thick (tens of nanometers) BP flake with different d_{BP} should exhibit constant Φ_{eff} for A_g^1 (A_g^2). Thus, the fitted $|c_{eff}|/|a_{eff}|$ and Φ_{eff} involve interplay of various anisotropy effects, distinct for different Raman modes and sensitive to d_{BP} , making it a challenge to

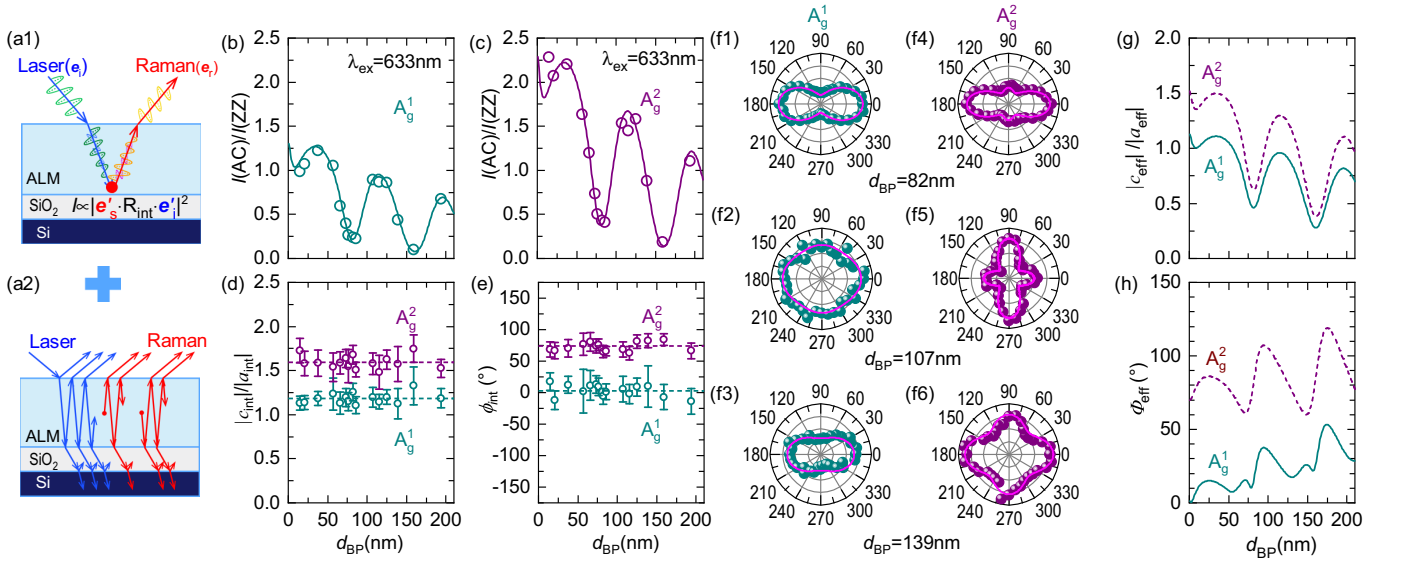


FIG. 2. (a1) Schematic diagram for propagation paths of incident laser (blue) and scattered Raman signal (red) in ALM and (a2) the interference effect of incident laser and scattered light within ALM/SiO₂/Si multilayer structure, the case of oblique incidence for convenience. $I(AC)/I(ZZ)$ of (b) A_g^1 and (c) A_g^2 modes with $\lambda_{ex}=633\text{nm}$. The solid lines are the fitted results. (d) $|c_{int}|/|a_{int}|$ and (e) ϕ_{int} (open circles) and their averaged values (dashed lines) of A_g^1 and A_g^2 modes versus d_{BP} . (f) ARPR intensity profiles of A_g^1 and A_g^2 modes in BP/90nm-SiO₂/Si with different d_{BP} , in which filled circles and pink lines are experimental and calculated results, respectively. (g) Predicted $|c_{eff}|/|a_{eff}|$ and (h) Φ_{eff} for A_g^1 and A_g^2 modes in BP flakes on 90nm-SiO₂/Si substrate.

predict the ARPR intensity of ALM flakes.

To tell apart various anisotropy effects on ARPR intensity of ALM flakes, as depicted in Fig.2(a1), the Raman scattering processes can be separated into the propagation paths of incident/scattered light and Raman scattering event at depth y . The latter is an inherent physical process governed by the anisotropic e-ph and e-phn couplings presented by \mathbf{R}_{int} (Section 2 of SM), $I(y) \propto |\mathbf{e}'_s(y) \cdot \mathbf{R}_{int} \cdot \mathbf{e}'_i(y)|^2$, in which $\mathbf{e}'_s(y)$ and $\mathbf{e}'_i(y)$ are modulated by birefringence and linear dichroism effects[5]. In addition, BP flakes commonly deposited onto SiO₂/Si substrate can generate a natural cavity due to the refractive index mismatch between BP flake and underlying substrate, where partial reflections of incident and scattered light occur at air/BP, BP/SiO₂ and SiO₂/Si interfaces (Fig.2(a2)). Multiple reflection and optical interference can further modulate both $\mathbf{e}'_s(y)$ and $\mathbf{e}'_i(y)$. These modulations arising from birefringence, linear dichroism and optical interference effects shows evident in-plane anisotropy, which can be described by the interference factor matrices of the incident laser ($J_i(y)$) and Raman signals ($J_s(y)$) at varied y using the transfer matrix method (TMM)[5, 20],

$$J_{i(s)}(y) = \begin{pmatrix} F_{i(s)X}(y) & 0 & 0 \\ 0 & 0 & 0 \\ 0 & 0 & F_{i(s)Z}(y) \end{pmatrix}. \quad (2)$$

where $F_{i(s)X}(y)$ and $F_{i(s)Z}(y)$ are respectively defined as the enhancement factors for incident laser (scattered sig-

nal) along X and Z axes, calculated by the TMM (Section 3 and Fig.S1 of SM[20]). Birefringence, linear dichroism and anisotropic interference effects are manifested in the different values of $F_{i(s)X}(y)$ and $F_{i(s)Z}(y)$ due to the varied complex refractive indexes along X (\tilde{n}_X) and Z (\tilde{n}_Z) axes. Thus, $\mathbf{e}'_i(y) = J_i(y)\mathbf{e}_i$ and $\mathbf{e}'_s(y) = \mathbf{e}_s J_s(y)$. And the measured Raman scattered intensity for a given phonon mode from BP flake is the integration of Raman signal over d_{BP} , expressed as follows,

$$I \propto \int_0^{d_{BP}} |\mathbf{e}_s J_s(y) \cdot \mathbf{R}_{int} \cdot J_i(y)\mathbf{e}_i|^2 dy. \quad (3)$$

We express the nonzero elements of \mathbf{R}_{int} for A_g modes of BP flakes as $R_{xx} = |a_{int}|e^{i\phi_a}$, $R_{zz} = |c_{int}|e^{i\phi_c}$ and $\phi_{int} = \phi_c - \phi_a$, then the Eq.3 becomes:

$$I \propto \int_0^{d_{BP}} |F_{iX}(y)F_{sX}(y)|a_{int}|e^{i\phi_a} \cos^2\theta + F_{iZ}(y)F_{sZ}(y)|c_{int}|e^{i\phi_c} \sin^2\theta|^2 dy. \quad (4)$$

Accordingly, $I(ZZ) \propto \int_0^{d_{BP}} |F_{iX}(y)F_{sX}(y)|a_{int}|^2 dy$ ($\theta = 0^\circ$) and $I(AC) \propto \int_0^{d_{BP}} |F_{iZ}(y)F_{sZ}(y)|c_{int}|^2 dy$ ($\theta = 90^\circ$). By fitting $I(AC)/I(ZZ)$ versus d_{BP} (Section 4 of SM), one can obtain \tilde{n}_x , \tilde{n}_z and $|c_{int}|/|a_{int}|$ for BP flakes. We summarized $I(AC)/I(ZZ)$ with excitation wavelength (λ_{ex}) of 633nm as a function of d_{BP} for A_g^1 and A_g^2 modes in Fig.2(b,c), respectively. The fitting of $I(AC)/I(ZZ)$ for these two modes are processed independently. The fitted \tilde{n}_X (\tilde{n}_Z) for A_g^1 and A_g^2 modes are almost identical

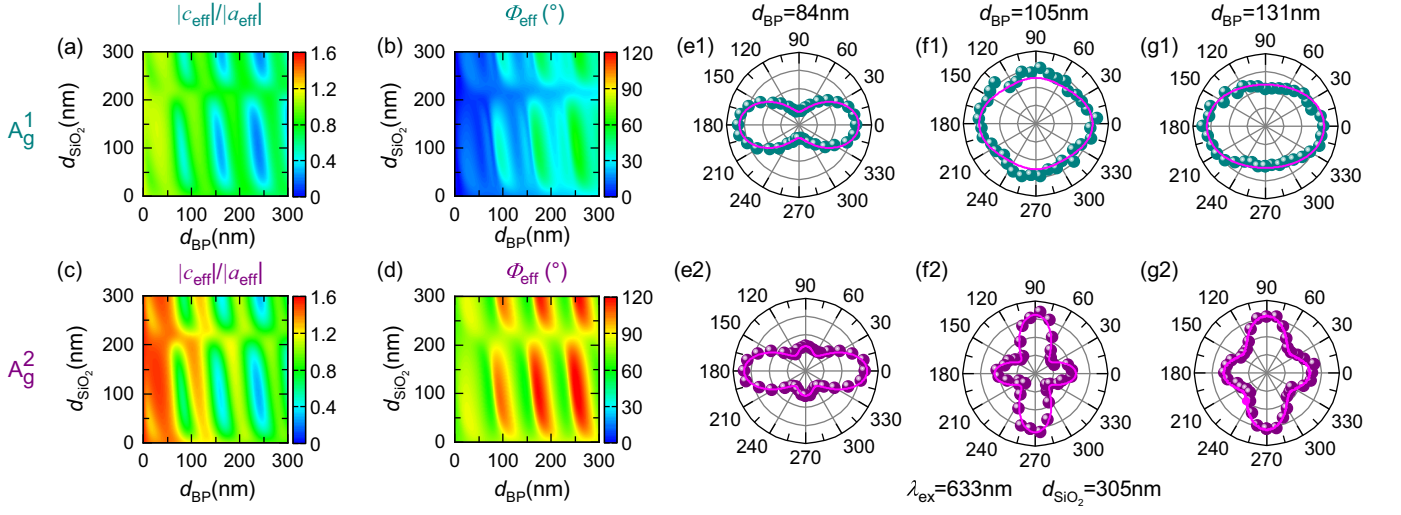


FIG. 3. (a,c) Predicted $|c_{\text{eff}}|/|a_{\text{eff}}|$ and (b,d) Φ_{eff} for A_g^1 and A_g^2 modes in BP flakes with varied d_{BP} and d_{SiO_2} for $\lambda_{\text{ex}}=633\text{nm}$. (e) Comparison of ARPR intensity profiles between the experimental (filled circles) and predicted (pink lines) results for A_g^1 and A_g^2 modes in BP flakes on 305nm-SiO₂/Si substrate, where the predicted curves are calculated by $|c_{\text{eff}}|/|a_{\text{eff}}|$ and Φ_{eff} in (a-d).

to each other, whose averaged values are summarized in Table I.

With the fitted \tilde{n}_X and \tilde{n}_Z , $F_{i(s)X}(y)$ and $F_{i(s)Z}(y)$ can be numerically calculated, and then $|c_{\text{int}}|/|a_{\text{int}}|$ and ϕ_{int} for the A_g^1 and A_g^2 modes in each BP flake can be determined by fitting the corresponding ARPR intensity in Fig.1(f) and Fig.S2 (Section 4 of SM), as illustrated in Figs.2(d,e), respectively. The average $|c_{\text{int}}|/|a_{\text{int}}|$ and ϕ_{int} of the A_g^1 and A_g^2 modes are used to calculate the ARPR intensity profile for BP flakes with varied d_{BP} (pink curves in Fig.2(f)), showing good agreement with the experimental ones.

The above constant $|c_{\text{int}}|/|a_{\text{int}}|$ and ϕ_{int} imply that the anisotropic e-pht ($H_{e-\text{pht}}$) and e-phn coupling ($H_{e-\text{phn}}$) matrices are almost unchanged for BP flakes ($d_{\text{BP}} > 20\text{nm}$), which can be ascribed to the similar electronic band structure[9]. In addition, $|c_{\text{int}}|/|a_{\text{int}}|$ for A_g^1 and A_g^2 modes are both larger than 1, indicating a larger $H_{e-\text{pht}(s)} \cdot H_{e-\text{phn}} \cdot H_{e-\text{pht}(i)}$ (Section 2 of SM) along Z axis than that along X axis owing to the much larger light absorption along Z axis[9, 24]. The larger $|c_{\text{int}}|/|a_{\text{int}}|$ of A_g^2 (~ 1.6) than A_g^1 (~ 1.18) mode implies that the ratio of $H_{e-\text{phn}}$ between the Z and X axes for A_g^2 mode is ~ 1.4 times of that for A_g^1 mode. Furthermore, the nonzero ϕ_{int} in \mathbf{R}_{int} for both A_g^1 and A_g^2 modes are induced by the anisotropic dielectric function due to the linear dichroism in BP flakes.

With the above insights into the modulations from birefringence, linear dichroism, anisotropic interference effects, and anisotropic e-pht (e-phn) coupling[9, 18] in Raman scattering process of BP flakes, we aim to integrate all these effects to derive the formalism of effective elements in \mathbf{R} to directly predict their ARPR response. By comparing the Eq.4 with the Eq.1, we can get the formalism for \mathbf{R} as follows(Section 5 of SM),

TABLE I. Complex refractive indexes \tilde{n} along $X(ZZ)$ and $Z(AC)$ axes of BP flakes at $\lambda_{\text{ex}}=633\text{nm}$, 532nm and 488nm.

Wavelength(nm)	\tilde{n}_X	\tilde{n}_Z
633	4.04+0.03i	3.95+0.33i
532	4.41+0.23i	4.09+0.67i
488	4.82+0.28i	4.50+0.74i

$$\frac{|c_{\text{eff}}|}{|a_{\text{eff}}|} = \left(\frac{|c_{\text{int}}|}{|a_{\text{int}}|} \right) \cdot \left(\frac{F_Z}{F_X} \right)$$

$$\Phi_{\text{eff}} = \arccos \left(\frac{\int_0^{d_{\text{BP}}} A_X A_Z \cos(\varphi_X - \varphi_Z + \phi_{\text{int}}) dy}{F_X F_Z} \right) \quad (5)$$

where $F_X = \sqrt{\int_0^{d_{\text{BP}}} A_X^2 dy}$ and $F_Z = \sqrt{\int_0^{d_{\text{BP}}} A_Z^2 dy}$ with A_X and A_Z the amplitudes of $F_{iX}(y)F_{sX}(y)$ and $F_{iZ}(y)F_{sZ}(y)$, respectively. φ_X and φ_Z are defined as the phases of $F_{iX}(y)F_{sX}(y)$ and $F_{iZ}(y)F_{sZ}(y)$, respectively. With these analysis, we numerically calculated $|c_{\text{eff}}|/|a_{\text{eff}}|$ and Φ_{eff} for A_g^1 and A_g^2 modes in BP flakes on 90nm-SiO₂/Si with $\lambda_{\text{ex}}=633\text{nm}$, as elucidated in Fig.2(g,h). Both $|c_{\text{eff}}|/|a_{\text{eff}}|$ and Φ_{eff} are sensitive to d_{BP} . With the derived \mathbf{R} with effective elements, one can predict the ARPR intensity for BP flakes. Good agreements between the predicted and experimental ARPR intensity for $\lambda_{\text{ex}}=633\text{nm}$ are shown in Fig.S3 of SM. The periodic variations of $|c_{\text{eff}}|/|a_{\text{eff}}|$ and Φ_{eff} of BP flakes give rise to periodic changes of the ARPR intensity shape. It is clear that the complicated dependencies of $|c_{\text{eff}}|/|a_{\text{eff}}|$ and Φ_{eff} on d_{BP} is the main reason for the challenge in predicting ARPR intensity for BP flakes in previous studies[6–9, 12, 16]. Similar derivation for \mathbf{R} can be applied to

other anisotropic ALM flakes to acquire a quantitative prediction of the ARPR response.

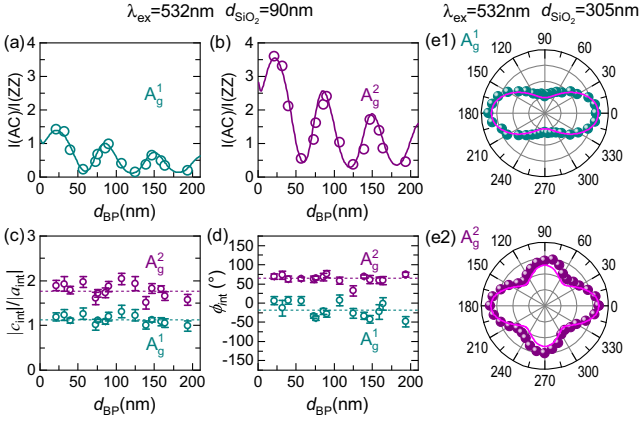


FIG. 4. $I(AC)/I(ZZ)$ of (a) A_g^1 and (b) A_g^2 modes of BP flakes on 90nm-SiO₂/Si with $\lambda_{ex}=532$ nm, (c) the corresponding $|c_{int}|/|a_{int}|$ and (d) ϕ_{int} versus d_{BP} . (e) Comparison of ARPR intensity profiles of A_g^1 and A_g^2 modes between the experimental (filled circles) and predicted (pink lines) results for BP flakes on 305nm-SiO₂/Si with $\lambda_{ex}=532$ nm.

Owing to the evident optical interference effect for the BP/SiO₂/Si multilayer structure, $|c_{eff}|/|a_{eff}|$ and Φ_{eff} are also sensitive to d_{SiO_2} . We plot the dependencies of $|c_{eff}|/|a_{eff}|$ and Φ_{eff} on d_{SiO_2} and d_{BP} for A_g^1 and A_g^2 modes in Fig.3(a-d). The $|c_{eff}|/|a_{eff}|$ ratio of A_g^1 mode consistently remains smaller than that of the A_g^2 mode. Similar behaviors are found for the Φ_{eff} . With these predicted $|c_{eff}|/|a_{eff}|$ and Φ_{eff} , the ARPR intensities for BP flakes on SiO₂/Si substrates with different d_{SiO_2} are also predictable, as exemplified by the ARPR intensity of BP flakes with $d_{BP}=84$ nm, 105nm and 131nm on 305nm-SiO₂/Si substrate in Figs.3(e-g). The predicted ARPR intensities well reproduce the measured ones.

To validate the universality of the above strategy for effective elements of \mathbf{R} to quantitatively predict the ARPR intensity in ALM flakes, we further measured the ARPR intensity for BP flakes under $\lambda_{ex}=532$ nm (Fig.4 and Fig.S4-6 of SM) and 488nm (Fig.S7-10 of SM). We summarize the $I(AC)/I(ZZ)$ for A_g^1 and A_g^2 modes in Figs.4(a,b) for $\lambda_{ex}=532$ nm. Similar to the case for $\lambda_{ex}=633$ nm, we fit the $I(AC)/I(ZZ)$ versus d_{BP} by using the Eq.4 to acquire \tilde{n}_X and \tilde{n}_Z for $\lambda_{ex}=532$ nm, as shown in Table I. By further fitting the ARPR intensity of A_g^1 and A_g^2 modes (Fig.S4 of SM) with Eq.4, we can obtain the elements ratio $|c_{int}|/|a_{int}|$ and phase difference ϕ_{int} in \mathbf{R}_{int} , as illustrated in Figs.4(c,d) for $\lambda_{ex}=532$ nm. We also calculate the effective element tensor ratio $|c_{eff}|/|a_{eff}|$ and phase difference Φ_{eff} in \mathbf{R} for BP flakes on SiO₂/Si substrate with varied d_{SiO_2} and d_{BP} based on the averaged values of $|c_{int}|/|a_{int}|$ and ϕ_{int} obtained above, which can successfully modeled the observed ARPR intensities of A_g^1 and A_g^2 modes for BP flakes without any additional fitting parameters, as exemplified the ones for BP flakes with $d_{BP}=105$ nm (also $d_{BP}=84$ nm and 131nm) on

305nm-SiO₂/Si substrate are shown in Fig.4(e) (in Fig.S6 of SM). The successful model for ARPR intensities of BP flakes with varying λ_{ex} and d_{SiO_2} by the predicted effective elements of \mathbf{R} suggests the general validity of our proposed strategy for \mathbf{R} of ALMs with effective and intrinsic elements.

The obtained \mathbf{R}_{int} for different λ_{ex} provides a new approach to study the anisotropic e-pht and e-phn coupling in ALM flakes. For example, the converse variation behaviors, i.e., continuous decrease (increase) in $|c_{int}|/|a_{int}|$ for A_g^1 (A_g^2) mode with λ_{ex} decreasing from 633nm to 488nm, imply that the e-phn coupling matrix ratio between AC and ZZ axes for the A_g^1 mode experiences opposite variation with decreasing λ_{ex} to that of the A_g^2 mode, due to the comparable e-pht coupling for the A_g^1 and A_g^2 modes under specific excitation. More insights into the anisotropy in e-pht and e-phn couplings could be derived by tracing the \mathbf{R}_{int} under varied laser excitations.

In conclusion, the Raman selection rule in BP flakes is influenced by anisotropy in both optics and e-pht/e-phn coupling, manifested through birefringence, linear dichroism, optical interference effects of multi-layer structures, and \mathbf{R}_{int} . Our proposed strategy to delineate the \mathbf{R}_{int} for phonon modes in BP flakes leads to a deeper understanding of the modulation of anisotropic effects on ARPR spectra in ALM flakes. By determining the effective Raman tensor elements of \mathbf{R} , we have been able to accurately predict the ARPR intensity profiles of the A_g^1 and A_g^2 modes in BP flakes on various substrates. This research overcomes the challenge in predicting ARPR intensity and provides a comprehensive insight into anisotropy and Raman scattering in ALM flakes.

We acknowledge the support from the Ministry of Science and Technology of China (Grant No. 2023YFA1407000), the Strategic Priority Research Program of CAS (Grant No. XDB0460000), National Natural Science Foundation of China (Grant Nos. 12322401, 12127807 and 12393832), CAS Key Research Program of Frontier Sciences (Grant No. ZDBS-LY-SLH004), Beijing Nova Program (Grant No. 20230484301), Youth Innovation Promotion Association, Chinese Academy of Sciences (No. 2023125) and CAS Project for Young Scientists in Basic Research (YSBR-026).

-
- [1] Loudon, R. The raman effect in crystals. *Adv. Phys.* **13**, 423–482 (1964).
 - [2] Cardona, M. (ed.) *Light Scattering in Solids I*, vol. 8 (Springer-Verlag, Berlin, 1983).
 - [3] Kranert, C., Sturm, C., Schmidt-Grund, R. & Grundmann, M. Raman tensor formalism for optically anisotropic crystals. *Phys. Rev. Lett.* **116**, 127401 (2016).
 - [4] Kranert, C., Sturm, C., Schmidt-Grund, R. & Grundmann, M. Raman tensor elements of β -Ga₂O₃. *Sci. Rep.* **6**, 35964 (2016).
 - [5] Lin, M.-L. *et al.* Understanding angle-resolved polarized

- raman scattering from black phosphorus at normal and oblique laser incidences. *Sci. Bull.* **65**, 1894–1900 (2020).
- [6] Ribeiro, H. B. *et al.* Unusual angular dependence of the Raman response in black phosphorus. *ACS Nano* **9**, 4270–4276 (2015).
- [7] Kim, J. *et al.* Anomalous polarization dependence of Raman scattering and crystallographic orientation of black phosphorus. *Nanoscale* **7**, 18708–18715 (2015).
- [8] Mao, N. *et al.* Birefringence-directed Raman selection rules in 2D black phosphorus crystals. *Small* **12**, 2627–2633 (2016).
- [9] Ling, X. *et al.* Anisotropic electron-photon and electron-phonon interactions in black phosphorus. *Nano Lett.* **16**, 2260–2267 (2016).
- [10] Phaneuf-L’Heureux, A.-L. *et al.* Polarization-resolved raman study of bulk-like and davydov-induced vibrational modes of exfoliated black phosphorus. *Nano Lett.* **16**, 7761–7767 (2016).
- [11] Zheng, W., Yan, J., Li, F. & Huang, F. Elucidation of ”phase difference” in raman tensor formalism. *Photon. Res.* **6**, 709–712 (2018).
- [12] Choi, Y. *et al.* Complete determination of the crystallographic orientation of ReX_2 ($X = \text{S}, \text{Se}$) by polarized raman spectroscopy. *Nanoscale Horiz.* **5**, 308–315 (2020).
- [13] Zhu, Y. *et al.* Raman tensor of layered black phosphorus. *Photonix* **1**, 17 (2020).
- [14] Pimenta, M. A., Resende, G. C., Ribeiro, H. B. & Carvalho, B. R. Polarized raman spectroscopy in low-symmetry 2d materials: angle-resolved experiments and complex number tensor elements. *Phys. Chem. Chem. Phys.* **23**, 27103–27123 (2021).
- [15] Zou, B. *et al.* Unambiguous determination of crystal orientation in black phosphorus by angle-resolved polarized raman spectroscopy. *Nanoscale Horiz.* **6**, 809–818 (2021).
- [16] Huang, S. *et al.* In-plane optical anisotropy of layered gallium telluride. *ACS Nano* **10**, 8964–8972 (2016).
- [17] Wu, J., Mao, N., Xie, L., Xu, H. & Zhang, J. Identifying the crystalline orientation of black phosphorus using angle-resolved polarized Raman spectroscopy. *Angew. Chem. Int. Ed.* **54**, 2366–2369 (2015).
- [18] Mao, N. *et al.* Direct observation of symmetry-dependent electron-phonon coupling in black phosphorus. *J. Am. Chem. Soc.* **141**, 18994–19001 (2019).
- [19] Strach, T., Brunen, J., Lederle, B., Zegenhagen, J. & Cardona, M. Determination of the phase difference between the Raman tensor elements of the A_{1g} -like phonons in $\text{SmBa}_2\text{Cu}_3\text{O}_{7-\delta}$. *Phys. Rev. B* **57**, 1292–1297 (1998).
- [20] Li, X.-L. *et al.* Layer number identification of intrinsic and defective multilayer graphenes by the Raman mode intensity from substrate. *Nanoscale* **7**, 8135–8141 (2015).
- [21] Ribeiro-Soares, J. *et al.* Group theory analysis of phonons in two-dimensional transition metal dichalcogenides. *Phys. Rev. B* **90**, 115438 (2014).
- [22] Wu, J.-B., Lin, M.-L., Cong, X., Liu, H.-N. & Tan, P.-H. Raman spectroscopy of graphene-based materials and its applications in related devices. *Chem. Soc. Rev.* **47**, 1822–1873 (2018).
- [23] Lin, M.-L. *et al.* Cross-dimensional electron-phonon coupling in van der Waals heterostructures. *Nat. Commun.* **10**, 2419 (2019).
- [24] Qiao, J., Kong, X., Hu, Z.-X., Yang, F. & Ji, W. High-mobility transport anisotropy and linear dichroism in few-layer black phosphorus. *Nat. Commun.* **5**, 4475 (2014).
- [25] Xia, F., Wang, H. & Jia, Y. Rediscovering black phosphorus as an anisotropic layered material for optoelectronics and electronics. *Nat. Commun.* **5**, 4458 (2014).
- [26] Luo, Z. *et al.* Anisotropic in-plane thermal conductivity observed in few-layer black phosphorus. *Nat. Commun.* **6**, 8572 (2015).
- [27] Schuster, R., Trinckauf, J., Habenicht, C., Knupfer, M. & Büchner, B. Anisotropic particle-hole excitations in black phosphorus. *Phys. Rev. Lett.* **115**, 026404 (2015).
- [28] Wang, S.-Y. *et al.* Tunable optical activity in twisted anisotropic two-dimensional materials. *ACS Nano* **17**, 16230–16238 (2023).
- [29] Dawson, P. Polarisation measurements in Raman spectroscopy. *Spectrochim. Acta Part A* **28**, 715–723 (1972).
- [30] Rulmont, A. & Flamme, J. Birefringence effect in the Raman spectrum of a crystal which is not cut parallel to the principal axes-I. *Spectrochim. Acta Part A* **35**, 629–633 (1979).
- [31] Rulmont, A., Flamme, J., Pottier, M. & Wanklyn, B. Birefringence effect in the Raman spectrum of a crystal which is not cut parallel to the principal axes-II. application to a single crystal of LaBO_3 . *Spectrochim. Acta Part A* **35**, 635–639 (1979).
- [32] Alonso-Gutiérrez, P., Sanjuán, M. L. & Morón, M. C. Raman selection rules in uniaxial media: The nonpolar modes of MnGa_2Se_4 . *Phys. Rev. B* **71**, 085205 (2005).
- [33] Zhang, H. *et al.* Cavity-enhanced linear dichroism in a van der waals antiferromagnet. *Nat. Photon.* **16**, 311–317 (2022).